

A Relativistic Explanation for the Darkness of Galactic Halos

(First draft - 03.08.2024)

Ramzi Suleiman¹²

¹Professor Emeritus, University of Haifa, Haifa, Israel

²CEO, Accura-c LTD, Haifa, Israel

Abstract

In this study, we extend previously established results of relativized Newtonian dynamics—originally derived for inertial rectilinear motion—to the context of a uniformly rotating disk. Our findings reveal the presence of a nonluminous component coexisting with the luminous component, with the ratio of their radial densities being solely dependent on the rotation velocity.

We apply these results to investigate the dynamics of both luminous and nonluminous matter in a diverse sample of 52 galaxies from the Spitzer Photometry & Accurate Rotation Curves (SPARC) dataset. For each galaxy, we calculate the radial density distributions of both matter components using only the measured rotation curves. The predicted radial density profiles of the nonluminous components closely trace the observed rotation curves for all tested galaxies.

Our analysis indicates that the nonluminous component begins to dominate over the luminous component at rotation velocity of approximately $\frac{V_{flat}}{3}$. At rotation velocities approaching V_{flat} , the luminous component nearly vanishes, with the majority of the matter being nonluminous. The nonluminous component is expected to strongly dominate in all tested galaxies, with a fraction ($0.757 \leq f_{NLM} \leq 0.990$, $\sigma_{f_{NLM}} = 0.0137$).

Moreover, consistent with the Radial Acceleration Relation (RAR), the correlations between the estimated total masses of the luminous and nonluminous components, and between the luminous component and the total dynamical mass, are very strong ($r = 0.947$ and 0.954 , respectively). Additionally, in agreement with the Baryonic Tully-Fisher Relation (BTFR), the correlation between the total luminous mass and V_{flat} is also substantial ($r = 0.626$).

These results suggest that key features typically attributed to exotic dark matter particles in galactic halos can be accounted for by simple relativistic considerations.

Keywords: Dark matter, nonluminous matter, dark matter in galaxies, matter-dark matter coupling, rotation curve, SPARC, Radial Acceleration Relation, Baryonic Tully-Fisher Relation.

Introduction

Compelling evidence suggests that galaxies are predominantly dominated by non-luminous (dark) matter, which resides primarily in their halos. This evidence is derived from various observational methods, including precise measurements of galaxies' rotation curves [1] [2] [3] [4] [5] [6] [7], gravitational lensing [8] [9] [10] [11] [12], and velocity dispersion measurements in elliptical galaxies [13] [14] [15].

In the Cold Dark Matter (CDM) paradigm, galaxies form when gas within dark matter (DM) halos cools and collapses towards the center of the DM potential well, creating a disc-like rotating structure that triggers star formation [7]. Dark matter candidates vary widely in mass, spanning over 90 orders of

magnitude from ultralight bosons to massive black holes [16] [17] [18] [19]. Among these, Weakly Interacting Massive Particles (WIMPs) are among the most studied candidates [20] [21] [22] [23]. While some candidates like neutrinos and axions are part of the standard model, most WIMP candidates, such as supersymmetric neutralinos and gravitinos, are beyond it. Additionally, baryonic matter in the form of brown dwarfs or massive compact halo objects (MACHOs) [24] [25] [26], including primordial black holes (PBHs) [27] [28], is considered as possible source of DM. For recent reviews on direct and indirect detection attempts of dark matter particles, see e.g., [29] [30] [31].

Despite the numerous dark matter candidates, none have been detected, and all remain highly speculative. This lack of detection is compounded by the fact that no single candidate can account for the total dark matter in the universe, and current searches have not significantly narrowed the hypothesized mass range.

Furthermore, the CDM model faces additional challenges. Computer simulations of galaxy evolution within the CDM framework do not always produce realistic galaxies. For example, the "cusp-core problem," particularly evident in low surface brightness disk galaxies and gas-rich dwarf galaxies, remains unresolved [32] [33].

A significant challenge to the CDM model is the recently discovered radial acceleration relation (RAR). Empirical data from numerous galaxies indicate that the total masses of baryonic and dark matter are strongly coupled, with the dark matter contribution to the dynamical mass being fully specified by the baryons [34] [35] [36] [37]. This coupling is not explained by the standard CDM paradigm. Scholz-Díaz et al. [38] addressed a related issue using data from 260 galaxies with spatially resolved optical spectra from the Calar Alto Legacy Integral Field Area (CALIFA) integral-field spectroscopic (IFS) survey [39]. They found that measured ages, metallicities, stellar angular momentum, morphology, and star formation rates correlate with both stellar and halo mass. Another challenge to the CDM paradigm is presented by Mistele et al. [40], who, using weak gravitational lensing data, found that the circular velocity curves of isolated galaxies remain flat out to hundreds of kiloparsecs, and potentially up to 1 Mpc, with no evidence of reaching the edge of a dark matter halo. Additionally, recent discoveries by the James Webb Space Telescope (JWST) of very massive galaxies at very early times post-Big Bang [41] [42] [43] contradict the CDM model's prediction of a decline in the number of massive galaxies at early cosmic times [44] [45].

In this study, we propose a relativistic approach to understanding the "darkness" of galaxies halos. Our main objective is to demonstrate that it is an observational effect due to galactic rotation rather than the presence of exotic dark matter clumps. Aided by basic principles, without any free parameters nor parametrized simulations, and based *only* on the measured rotation curves of disk-shaped galaxies, we derive predictions for the radial distributions of luminous and non-luminous matter, their respective energy distributions, total amounts within the probed ranges, and the fraction of non-luminous matter relative to the total matter. We show that the derived predictions align well with the well-confirmed characteristics of nonluminous matter in galaxies, including its dominance over luminous matter, concentration in galaxies' outskirts, and tight coupling with luminous matter.

In the following sections, we introduce the key features of our relativistic model and derive mathematical expressions for the densities and energy densities of luminous and non-luminous matter in a circularly rotating disk (Section 2). In Section 3, we apply the derived results to a diverse sample of 52 rotationally supported galaxies from the Spitzer Photometry & Accurate Rotation Curves (SPARC) database [34] [35]. For each individual galaxy we construct the radial density distributions of the luminous and nonluminous matter components, calculate their total amounts and their relative fractions out of the total dynamical mass, and confront these results with confirmed characteristics of nonluminous matter in galaxies and its coupling with the luminous matter. In section 4 we summarize and conclude.

2. Theory

We utilize two theoretical results derived in previously published papers: One on the relativistic dependence of the luminosity of matter in rectilinear inertial motion [46] [47]. The second set extends this result to account for bodies in circular motion [48].

For the case of inertial rectilinear motion, we found that the relativistic densities of the luminous and nonluminous matter of a receding homogeneous body with rest density ρ_0 , as functions of the body's departure velocity, relative to a stationary observer, are given by:

$$\rho_{LM} = \frac{1-\beta}{1+\beta} \rho_0 \quad (1)$$

$$\rho_{NLM} = \frac{2\beta}{1+\beta} \rho_0 \quad (2)$$

Where ρ_{LM} and ρ_{NLM} denote the densities of the luminous (observable) and the nonluminous (unobservable) matter, respectively, $\beta = \frac{v}{V_c}$, where v is the recession velocity of the body relative to the stationary observer, and V_c is the velocity of the information carrier received by the observer from the moving body. The only constraint put on V_c is $V_c > v$. It stems from practical considerations; otherwise, the carrier will not reach the observer's reference frame. It is important to stress that equations (1) and (2) are valid for any information carrier if its velocity exceeds the velocity of the receding body.

As shown by equations (1) and (2), *the predicted densities of the luminous and nonluminous matter components are determined solely by the dimensionless velocity β* . The equations prescribe that the two component co-exist in a dynamic duality, with luminous matter density decreasing, and nonluminous matter density increasing with increase in β , and vice versa. For any velocity β we have:

$$\rho_{NL} + \rho_{NLM} = \rho_0 \quad (3)$$

The energy densities of the luminous and nonluminous components are given by (see, e.g., [34]):

$$e_{LM} = \frac{1-\beta}{1+\beta} \beta^2 e_0 \quad (4)$$

And

$$e_{NLM} = \frac{2\beta^3}{1+\beta} e_0 \quad (5)$$

Where e_0 is the matter energy density at the rest- (nonrotating) frame, given by the Newtonian term $e_0 = \frac{1}{2} \rho_0 \beta^2$.

Application of the proposed relativistic model to the cosmology of the universe was successful in predicting, and explaining in physical terms, many observationally confirmed astrophysical and cosmological phenomena. Most importantly, the model suggests an intriguing inference about the nature of dark energy, being the energy of the intergalactic dark matter of the receding universe [46] [47] [49]. The model also predicts and explains the GZK cutoff limit to the cosmic-ray energy spectrum, the coincidence problem, and the deceleration-acceleration transition redshift [47]. For the quantum scale, the model predicts and explains several phenomena including matter-wave duality, quantum phase

transition, and quantum criticality [46] [49], quantum entanglement [50], and the diffraction of particles in the double slit experiment [51].

To extend proposed relativistic model to the case of circular motion, we utilize a previously proven result in [48], indicating that the circular and rectilinear motion are *dynamically equivalent* [52] [53], namely, that the equations describing the dynamics in both systems are mathematically identical. Interestingly, for the case of inertial motion, this result is in complete agreement with Galileo’s interpretation of inertia. In Galileo’s words: “All external impediments removed, a heavy body on a spherical surface concentric with the earth will maintain itself in that state in which it has been; if placed in movement toward the west (for example), it will maintain itself in that movement” [54]. This type of “circular inertia” or “horizontal circular inertia” was a precursor to Newton’s notion of rectilinear inertia [55]. As we shall see hereafter, the inclusion of uniform rotational motion under the umbrella of inertial motion proves very instrumental in exploring the luminous and nonluminous matter distribution, and their interdependent dynamics in galaxies.

The dynamical equations for a uniformly rotating disk

To derive the relativistic expressions for the luminous and nonluminous components of matter in a uniformly rotating homogeneous disk with rest-mass density ρ_0 and rest radius of R_0 (see Figure 1), we utilize the dynamical equivalence between rectilinear and rotational motion. From the standpoint of a nonrotating observer, the dynamical equations for the densities of the luminous (observable) and nonluminous (unobservable) matter components, and their respective energy densities at radius r can be written directly from equations (1) - (5) as:

$$\frac{\rho(r)_{LM}}{\rho_0} = \frac{1-\beta(r)}{1+\beta(r)} \quad (6)$$

$$\frac{\rho(r)_{NLM}}{\rho_0} = \frac{2\beta(r)}{1+\beta(r)}, \quad (7)$$

$$\rho(r)_{LM} + \rho(r)_{NLM} = \rho_0 \quad (8)$$

$$\frac{e_{LM}(r)}{e_0} = \frac{1-\beta(r)}{1+\beta(r)} \beta^2(r) \quad (9)$$

$$\frac{e_{NLM}(r)}{e_0} = \frac{2\beta^3(r)}{1+\beta(r)} \quad (10)$$

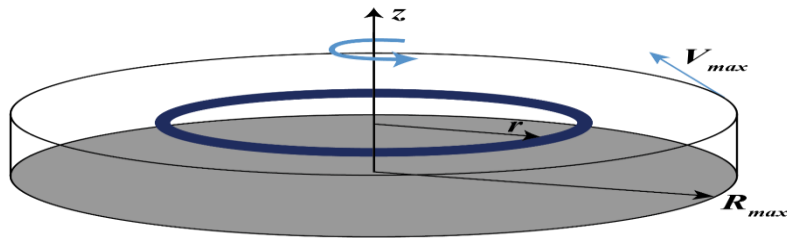


Figure 1. A uniformly rotating disk.

The model described by equations (6) - (10) uncovers new fundamental parameters which could be easily tested. First, the rotation velocity β_{eq} at which the densities of the luminous and nonluminous components are predicted to be equal should satisfy:

$$\frac{1-\beta_{eq}}{1+\beta_{eq}} \beta_{eq}^2 = \frac{2\beta_{eq}^3}{1+\beta_{eq}} \quad (11)$$

Which for $\beta \neq 0$ solves for:

$$\beta_{eq} = \frac{1}{3} \quad (12)$$

For $\beta < \frac{1}{3}$ the luminous matter component is predicted to dominate over the nonluminous component for velocities satisfying, while for $\beta > \frac{1}{3}$ the nonluminous matter is predicted to dominate.

Another intriguing symmetry emerges at $\beta = \frac{1}{2}$, at which the from equations (6) and (7) we get: $\frac{\rho_{LM}}{\rho_0} = \frac{1}{3}$, and $\frac{\rho_{LM}}{\rho_0} = \frac{2}{3}$.

Furthermore, the predicted luminous matter energy density has a unique maximum. Deriving the expression in eq. 9 with regard to β and equating the derivative to zero, we get:

$$\frac{\partial \frac{e_{LM}(r)}{e_0}}{\partial x} = \frac{2\beta(r)(\beta^2(r) + \beta(r) - 1)}{(1+\beta(r))^2} = 0 \quad (13)$$

Yielding:

$$\beta^2(r) + \beta(r) - 1 = 0 \quad (14)$$

Which solves for:

$$\beta_{LM_{max}} = \frac{\sqrt{5}-1}{2} = \varphi \approx 0.618 \quad (15)$$

Where φ is the famous golden ratio [56]. The maximal luminous matter energy density is equal to:

$$e_{LM_{max}} = \frac{1-\varphi}{1+\varphi} \varphi^2 e_0 = \varphi^5 e_0 \approx 0.09016994 e_0. \quad (16)$$

And the nonluminous matter energy density at $\beta = \varphi$ equals:

$$e_{NLM}(\beta = \varphi) = e_0 \frac{2\varphi^3}{1+\varphi} = 2\varphi^4 e_0 \approx 0.29179607 e_0 \quad (17)$$

The mathematical beauty of the above equations is impressive. The emergence of the golden ratio φ (≈ 0.618) as the dimensionless rotation velocity $\frac{v}{v_{max}}$, at which the luminous energy density reaches its maximal value (of $\varphi^5 e_0$), adds to numerous discoveries of the golden ratio in almost all fields of science, technology and the arts, including in the structure of plants [57], quantum matter [58] [59], atomic physics [60], and astronomy [61] (for recent reviews see [62] and [63]).

3. Predicting the radial distributions of luminous and nonluminous matter components and their fractions in disk galaxies

We demonstrate the application of relativistic model derived above for predicting the radial distributions of the luminous and nonluminous matter densities and their respective fractions in disk-shaped galaxies.

The accuracy of predictions should be taken with a grain of salt due to the simplifications made in the model. In real galaxies, the density of matter ρ_0 is rarely homogeneous, their morphologies are not completely disk-shaped, and their rotation is not circular. Our main concern here is to show that despite its simplifying assumptions, the proposed relativistic model uncovers what we know about nonluminous matter in galaxies, and its dynamical interconnectedness with their luminous matter, including the domination of the nonluminous matter over the luminous matter, its concentration, predominantly, in the galaxies' halos, and its tight coupling with ordinary matter. For this purpose, we utilized the rotation curves of a sizable diverse sample of 52 galaxies from the SPARC database [34] [35]. which includes 175 disk galaxies with homogeneous surface photometry and high-quality HI/H α rotation curves, spanning a wide range of morphological types, stellar masses, surface brightness, gas fractions, and Hubble types. We start by describing, step-by-step, the calculations for the nearby galaxy NGC 3741 as an example. We then depict the results for the remaining selected sample using the same method, and underscore their emerging main features.

Galaxy NGC 3741 is an extremely gas-rich and highly nonluminous matter-dominated dwarf galaxy [64] [65]. It is located at distance $D= 3.21\text{Mpc}$. Its total matter mass is about $4.03 \times 10^9 M_{\odot}$, and its nonluminous matter halo mass is about $7.657 \times 10^{10} M_{\odot}$. It has an effective radius of $r_e=0.32$ kpc and a maximal rotation velocity of 51.6 km s^{-1} . The galaxy's SPARC data for the radial distance (in kpc), and the respective rotation velocity (in km. s^{-1}) are depicted in the first two columns of Table 1. The third column depicts the normalized velocity $\beta = \frac{v(r)}{V_{max}}$, where V_{max} is the maximal measured velocity, equaling 51.6 km.s^{-1} . The fourth column depicts the predicted relative radial density distribution of the nonluminous matter component ($\frac{\rho_{NLM}(r)}{\rho_0}$) calculated from the rotational curve data using eq. 7. The relative radial density distribution of the luminous matter, $\frac{\rho_{LM}(r)}{\rho_0}$ (omitted from the table), is simply $1 - \frac{\rho_{NLM}(r)}{\rho_0}$. The fifth column depicts the luminous matter energy density, calculated from the rotational curve data using equation 9. The predicted matter density distributions, alongside with the normalized rotation velocity, are depicted in Figure 2.

Inspection of Figure 2 reveals several interesting features: 1. In agreement with observations, the galaxy is dominated by nonluminous matter component. The predicted density of the nonluminous (luminous) matter increases (decreases) with the distance from the galaxy's center. 2. In agreement with observations, the bulk of nonluminous matter resides at the outer regions of the galaxy. For distances $r < 0.464$ kpc from the center of the galaxy, the luminous matter component is predicted to dominate the galaxy, while for $r > 0.464$ it is dominated by the nonluminous component. 3. Intriguingly, the predicted nonluminous matter density profile is an almost exact tracer of the galaxy's measured rotation velocity (with significant large positive Pearson correlation coefficient, $(r(19) = .991, p < .001)$).

Table 1. Galaxy NGC 3741. Measured rotation velocities and the calculated nonluminous matter density, and its energy density as functions of r

r kpc	$v(r)$ km.s ⁻¹	$v(r)/V_{max}$	$\rho_{NLM}(r)$ ρ_0	$e_{LM}(r)$ e_0
0.23	13.1	0.2538760	0.4049459	0.0383530
0.47	17.3	0.3352713	0.5021770	0.0559587
0.7	23.6	0.4573643	0.6276596	0.0778870
0.93	26.2	0.5077520	0.6735219	0.0841700
1.17	27.4	0.5310078	0.6936709	0.0863754
1.4	26.9	0.5213178	0.6853503	0.0855131
1.64	27.4	0.5310078	0.6936709	0.0863754
1.87	31.0	0.6007752	0.7506053	0.0900142
2.1	32.5	0.6298450	0.7728894	0.0900958
2.33	33.0	0.6395349	0.7801418	0.0899231
2.57	36.5	0.7073643	0.8286039	0.0857605
2.8	38.9	0.7538760	0.8596685	0.0797545
3.26	41.5	0.8042636	0.8915145	0.0701728
3.73	42.7	0.8275194	0.9056204	0.0646301
4.21	44.7	0.8662791	0.9283489	0.0537698
4.67	46.7	0.9050388	0.9501526	0.0408298
5.14	48.5	0.939922481	0.9690310	0.0273597
5.61	50.0	0.968992248	0.9842520	0.0147866
6.07	50.2	0.972868217	0.9862476	0.0130163
6.54	50.1	0.970930233	0.9852508	0.0139042
7	51.6	1	1	0

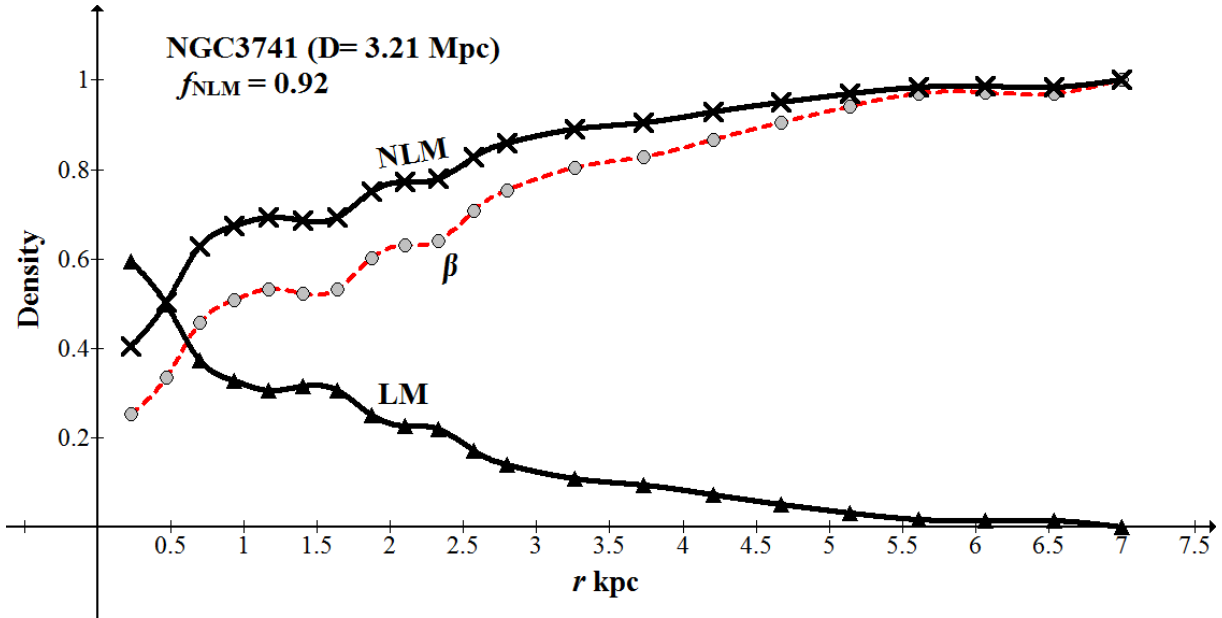


Figure 2. Predicted luminous and nonluminous matter density distributions in NGC 3741.

In addition, from Table 1 and Fig. 2, we find that the rotation velocity reaches $\frac{v(r)}{V_{max}} = \frac{1}{3}$ at radius of about $r \approx 0.464$ kpc, which is indeed the point of intersection between the profiles of the luminous and nonluminous matter densities as predicted (see equations 11 and 12). Also, the prediction of maximal luminous matter density at $\frac{v(r)}{V_{max}} = \varphi \approx 0.618$ (see equations 15 and 16) is confirmed. As

shown in the table, $\frac{e_{LM}(r)}{e_0}$ reaches a maximum of ≈ 0.0901 at $r = 2.1$ kpc, at which the measured rotation velocity is $\approx 0.63 V_{max}$, which is very close to the predicted velocity.

The total amounts of luminous and nonluminous matter within two galactocentric radii r_1, r_2 , ($r_2 > r_1$), could be obtained, respectively, by integrating equations (5) and (6) with respect to r :

$$M_{LM}(r_1, r_2) = \int_{r_1}^{r_2} 2\pi r \rho(r)_{LM} dr = 2\pi\rho_0 \int_{r_1}^{r_2} \frac{1-\beta(r)}{1+\beta(r)} r dr \quad (18)$$

and

$$M_{NLM}(r_1, r_2) = \int_{r_1}^{r_2} 2\pi r \rho(r)_{NLM} dr = 2\pi\rho_0 \int_{r_1}^{r_2} \frac{2\beta(r)}{1+\beta(r)} r dr \quad (19)$$

From equations (18) and (19), the predicted total mass within (r_1, r_2) is equal to:

$$\begin{aligned} M_{tot}(r_1, r_2) &= M_{LM}(r_1, r_2) + M_{NLM}(r_1, r_2) = 2\pi\rho_0 \int_{r_1}^{r_2} \left(\frac{1-\beta(r)}{1+\beta(r)} + \frac{2\beta(r)}{1+\beta(r)} \right) r dr \\ &= \pi\rho_0 (r_2^2 - r_1^2) \end{aligned} \quad (20)$$

And the fraction of nonluminous matter within (r_1, r_2) is:

$$f_{NLM}(r_1, r_2) = \frac{M_{NLM}}{M_{tot}} = \frac{2\pi\rho_0 \int_{r_1}^{r_2} \frac{2\beta(r)}{1+\beta(r)} r dr}{\pi\rho_0 (r_2^2 - r_1^2)} = \frac{4}{(r_2^2 - r_1^2)} \int_{r_1}^{r_2} \frac{\beta(r)}{1+\beta(r)} r dr \quad (21)$$

To calculate the predicted nonluminous matter fraction in NGC 3741, we performed a numerical integration of the expression in eq. (21) over the range $r_{min} = 0.23$ kpc and $r_{max} = 7$ kpc. For this purpose, we utilized the aria calculation utility option provided by the plotter program Graph [66], a free online utility by which the figures were drawn. The resulting fraction is $f_{NLM}(0.23, 7) = 0.92374675044 \approx 0.92$. The comparable fraction based on the results reported in [64] and [65] is equal to $\frac{7.657 \times 10^{10} M_\odot}{4.03 \times 10^9 M_\odot + 7.657 \times 10^{10} M_\odot} = 0.95$, which differs from the predicted value by less than 3%.

Using the same procedure, we calculated the luminous and nonluminous matter density distributions, and total fraction, for another 51 galaxies selected at random from SPARC. The resulting radial distributions of luminous and nonluminous matter densities for subsample of 6 galaxies, alongside with their respective measured rotational curve are depicted in Figure 3, and the distributions for all the 52 galaxies appear in Appendix A.

Table 2 depicts basic parameters of the investigated galaxies. As shown in the table, the selected sample is quite diverse in terms of the distance ($2.08 \leq D \leq 96.8$, $\bar{D} = 26.61$, $\sigma_D = 27.62$, in Mpc), the probed range ($2.56 \leq R \leq 69.62$, $\bar{R} = 14.98$, $\sigma_R = 14.64$, in kpc), and maximal rotation velocity ($25 \leq V_{max} \leq 321$, $\bar{V}_{max} = 106.82$, $\sigma_{V_{max}} = 69.27$, in km.s^{-1}).

A major result of our relativistic approach is the uncovered dynamical duality between the luminous and the nonluminous matter components that is governed solely by the dimensionless velocity β (see equations. (6) and (7)). As evident from the plots in Fig. 3 and Appendix A. This dynamic is manifest for all the investigated galaxies, with the nonluminous component increasing with velocity and dominating at higher velocities. In the proposed model, the halo of each galaxy emerges naturally from the dependencies of the luminous and nonluminous matter on the dimensionless velocity β . The tight coupling between the nonluminous and luminous matter, prescribed by the model, is revealed vividly in all the plots, where the density profiles of the nonluminous matter is a faithful trace to the rotation velocity of the probed luminous matter.

Table 3 depicts the estimated distance D (2nd row) and the measured maximal velocity V_{max} for every selected galaxy (3rd row), alongside with the model's main predictions approximated to three numbers after the decimal point: Rows (4)-(6) depict, within the probed radii range, the calculated estimates of the masses of luminous, nonluminous, and total matter M_{LM} , M_{NLM} , and M_{tot} (scaled by $2\pi\rho_0$). Row (7) depicts the estimated fraction of nonluminous matter (f_{NLM}), and row (8) depicts the Pearson correlation coefficients between the estimated density profile of nonluminous matter, and the measured rotation velocity profile. The calculations of M_{LM} , M_{NLM} , M_{tot} , and f_{NLM} , were performed by numerical integration on equations (18) - (21), respectively, using the free online program Graph. As could be seen in the table, all the tested galaxies are strongly dominated by their nonluminous components ($0.757 \leq f_{NLM} \leq 0.990$, $\overline{f_{NLM}} = 0.9394$, $\sigma_{f_{NLM}} = 0.0137$). In addition, as shown in the far-right column in Table 3, for all the investigated galaxies the correlation between the measured rotation velocities $v(r)$ and the predicted nonluminous matter density $\rho_{NLM}(r)$ is very high (mean = 0.9914, $\sigma = 0.0057$).

The model prescribes that the correlation between the luminous matter, and the nonluminous and total matter should be unity (see equation (8)). A Pearson correlation between the calculated values of M_{LM} and M_{NLM} yields $r(50) = .947$, $p < .001$, and between M_{LM} and M_{tot} yields $r(50) = .954$, $p < .001$ (see figures 4 and 5). The results also uncover the Baryonic Tully-Fisher relation [67] [68]: The Pearson correlations between M_{LM} and V_{max} is quite high ($r(50) = .626$, $p < .001$). A similarly high correlation ($r(50) = .70$, $p < .001$) is obtained between M_{NLM} and V_{max} , which should not be surprising given the tight coupling between the luminous and nonluminous matter components (see equations 6 and 7). The correlations of the fraction of nonluminous matter, f_{NLM} , with V_{max} , with the distance D , and with the range of observations, were small and non-significant ($r = .197$, $p = .161$, $r = .223$, $p = .112$, and $r = .247$, $p = .077$, respectively).

Table 2. Basic parameters for the investigated SPARC galaxies.

#	Galaxy (1)	D Mpc (2)	r_{min} Kpc (3)	r_{max} Kpc (4)	Range Kpc (5)	n (6)	V_{max} Km/s. (7)
1	D564-8	8.79	0.51	3.07	2.56	6	25.00
2	D631-7	7.72	0.45	7.19	6.74	16	58.50
3	DDO064	6.80	0.1	2.98	2.97	14	46.90
4	DDO154	4.04	0.49	5.92	5.43	12	48.20
5	DDO161	7.50	0.6	13.37	12.77	31	66.80
6	DDO168	4.25	0.41	4.12	3.71	10	55.00
7	DDO170	15.4	1.87	12.33	10.46	8	62.2
8	ESO079-G014	28.70	0.41	16.67	16.26	15	178.00
9	ESO116-G012	13.00	0.25	9.86	9.61	15	112.00
10	ESO444-G084	4.83	0.26	4.44	4.18	7	63.10
11	ESO563-G021	60.80	0.45	42.41	41.96	30	321.00
12	F561-1	66.4	1.61	9.66	8.05	6	50.40
13	F563-1	48.90	1.07	20.1	19.03	17	112.50
14	F563-V1	54.00	1.31	7.87	6.56	6	29.50

15	F563-V2	59.70	0.28	10.47	10.19	10	118.00
16	F565-V2	51.80	1.26	8.80	7.54	7	83.10
17	F567-2	79.00	1.92	9.59	7.67	5	52.20
18	F568-1	90.70	0.44	13.23	12.79	12	142.00
19	F568-V1	80.60	0.39	17.63	17.24	15	118.00
20	F568-3	82.40	0.64	17.98	17.34	18	120.00
21	F571-8	53.30	0.22	15.55	15.33	13	144.00
22	F574-1	96.80	0.47	12.6	12.13	14	99.70
23	F583-1	35.40	0.26	16.26	16.00	25	86.90
24	F583-4	53.30	0.22	7.29	7.07	12	69.90
25	IC2574	3.91	0.85	10.23	9.38	34	67.50
26	KK98-251	6.80	0.25	3.13	2.88	15	34.60
27	NGC0024	7.30	0.21	11.27	11.06	29	110.00
28	NGC0055	2.11	1.23	13.5	12.27	21	87.40
29	NGC0100	13.5	0.23	9.62	9.39	21	91.20
30	NGC0247	3.7	1.08	14.54	13.46	26	108.00
31	NGC0289	20.8	1.5	71.12	69.62	28	194.00
32	NGC0300	2.08	0.91	11.80	10.89	25	97.00
33	NGC1705	5.73	0.22	6.00	5.78	14	73.20
34	NGC2366	3.27	0.12	6.06	5.94	26	53.70
35	NGC2403	3.16	0.16	20.87	20.71	73	136.00
36	NGC2915	4.06	0.34	10.04	9.70	30	86.50
37	NGC 3741	3.21	0.23	7.00	6.77	21	51.60
38	NGC3769	18.00	1.74	37.16	35.42	12	126.00
39	NGC6503	6.26	0.76	23.50	22.74	24	118.00
40	NGC7793	3.61	0.11	7.87	7.76	46	116.00
41	NGC7814	14.40	0.63	14.4	13.77	18	265.00
42	UGC0750	58.70	0.31	22.85	22.54	11	78.90
43	UGC02953	16.50	0.09	62.39	62.30	114	319.00
44	UGC03205	50.00	0.28	40.04	39.76	48	237.00
45	UGC05253	22.90	0.13	53.29	53.16	73	248.00
46	UGC05414	9.40	0.68	4.11	3.43	6	61.40
47	UGC05716	21.30	1.03	12.37	11.34	12	74.70

48	UGC05721	6.18	0.09	6.74	6.65	23	82.60
49	UGC05764	7.47	0.36	3.62	3.26	10	55.80
50	UGC05829	8.64	0.63	6.91	6.28	11	68.60
51	UGC08699	39.30	0.22	25.70	25.48	41	202.00
52	UGC08837	7.21	0.52	4.20	3.68	8	48.00

(1) galaxy name, (2) distance from us, (3) and (4), the minimum and maximum probed radii, respectively, (5) the probed range (6) number of measurements, (7) maximal rotation velocity.

Table 3. Estimated distance, maximal measured velocity, and main results for 52 selected SPARC galaxies.

#	Galaxy (1)	D Mpc (2)	V_{max} Km/s. (3)	M_{LM} (4)	M_{NLM} (5)	f_{NLM} (6)	$corr(\rho_{NLM}, v)$ (7)
1	D564-8	8.79	25.00	0.379	4.203	0.917	0.994
2	D631-7	7.72	58.50	2.137	23.610	0.917	0.986
3	DDO064	6.80	46.90	0.348	4.087	0.921	0.990
4	DDO154	4.04	48.20	1.031	16.373	0.941	0.993
5	DDO161	7.50	66.80	5.380	83.844	0.940	0.992
6	DDO168	4.25	55.00	0.652	7.751	0.870	0.969
7	DDO170	15.4	62.20	3.640	70.626	0.951	0.997
8	ESO079-G014	28.70	178.00	9.679	129.182	0.930	0.991
9	ESO116-G012	13.00	112.00	2.170	46.409	0.955	0.990
10	ESO444-G084	4.83	63.10	0.409	9.414	0.958	0.992
11	ESO563-G021	60.80	321.00	17.560	881.643	0.980	0.989
12	F561-1	66.40	50.40	1.562	43.800	0.966	0.997
13	F563-1	48.90	112.5	7.830	193.603	0.961	0.989
14	F563-V1	54.00	29.50	1.304	28.807	0.957	0.997
15	F563-V2	59.7	118.00	1.603	53.168	0.971	0.987
16	F565-V2	51.8	83.10	3.779	34.147	0.900	0.992
17	F567-2	79.00	52.20	2.097	42.043	0.952	0.999
18	F568-1	90.70	142.00	5.843	81.577	0.933	0.987
19	F568-V1	80.6	118.00	4.193	151.139	0.973	0.989
20	F568-3	82.40	120.00	14.018	147.417	0.913	0.987
21	F571-8	53.30	144.00	6.473	114.404	0.946	0.984

22	F574-1	96.80	99.70	3.435	75.835	0.957	0.989
23	F583-1	35.40	86.90	5.606	126.554	0.958	0.988
24	F583-4	53.30	69.90	2.505	24.043	0.906	0.989
25	IC2574	3.91	67.50	2.275	7.105	0.757	0.988
26	KK98-251	6.80	34.60	0.532	4.335	0.891	0.988
27	NGC0024	7.30	110.00	1.290	62.194	0.980	0.989
28	NGC0055	2.11	87.4	4.372	86.000	0.952	0.994
29	NGC0100	13.5	91.20	3.590	42.656	0.922	0.985
30	NGC0247	3.7	108.00	7.498	97.625	0.929	0.992
31	NGC0289	20.8	194.00	160.957	2366.945	0.936	0.999
32	NGC0300	2.08	97.00	3.646	65.560	0.947	0.994
33	NGC1705	5.73	73.20	0.215	17.761	0.988	0.999
34	NGC2366	3.27	53.70	1.262	17.093	0.931	0.989
35	NGC2403	3.16	136.00	4.649	213.117	0.979	0.987
36	NGC2915	4.06	86.50	1.859	48.484	0.963	0.991
37	NGC 3741	3.21	51.60	1.866	22.607	0.924	0.991
38	NGC3769	18.00	126.00	17.488	671.431	0.975	0.999
39	NGC6503	6.26	118.00	2.786	273.129	0.990	0.999
40	NGC7793	3.61	116.00	2.196	28.766	0.929	0.986
41	NGC7814	14.40	265.00	18.521	171.991	0.903	0.999
42	UGC0750	58.70	78.90	8.901	252.113	0.966	0.982
43	UGC02953	16.50	319.00	162.928	1783.324	0.916	0.999
44	UGC03205	50.00	237.00	36.979	764.583	0.954	0.997
45	UGC05253	22.90	248.00	69.584	1350.319	0.961	0.999
46	UGC05414	9.40	61.40	0.831	7.384	0.899	0.994
47	UGC05716	21.30	74.70	2.908	73.070	0.962	0.997
48	UGC05721	6.18	82.60	0.629	22.081	0.972	0.988
49	UGC05764	7.47	55.80	0.356	6.132	0.945	0.996
50	UGC05829	8.64	68.60	3.147	20.528	0.867	0.988
51	UGC08699	39.30	202.00	18.647	311.574	0.944	0.999
52	UGC08837	7.21	48.00	1.337	7.348	0.846	0.989

- (1) galaxy name, (2) distance from us, (3) maximal rotation velocity, (4) and (5) predicted total mass of the luminous and nonluminous component, respectively (6) predicted fraction of the nonluminous component, (7) Pearson correlations between the measured radial velocities $v(r)$ and the nonluminous component density.

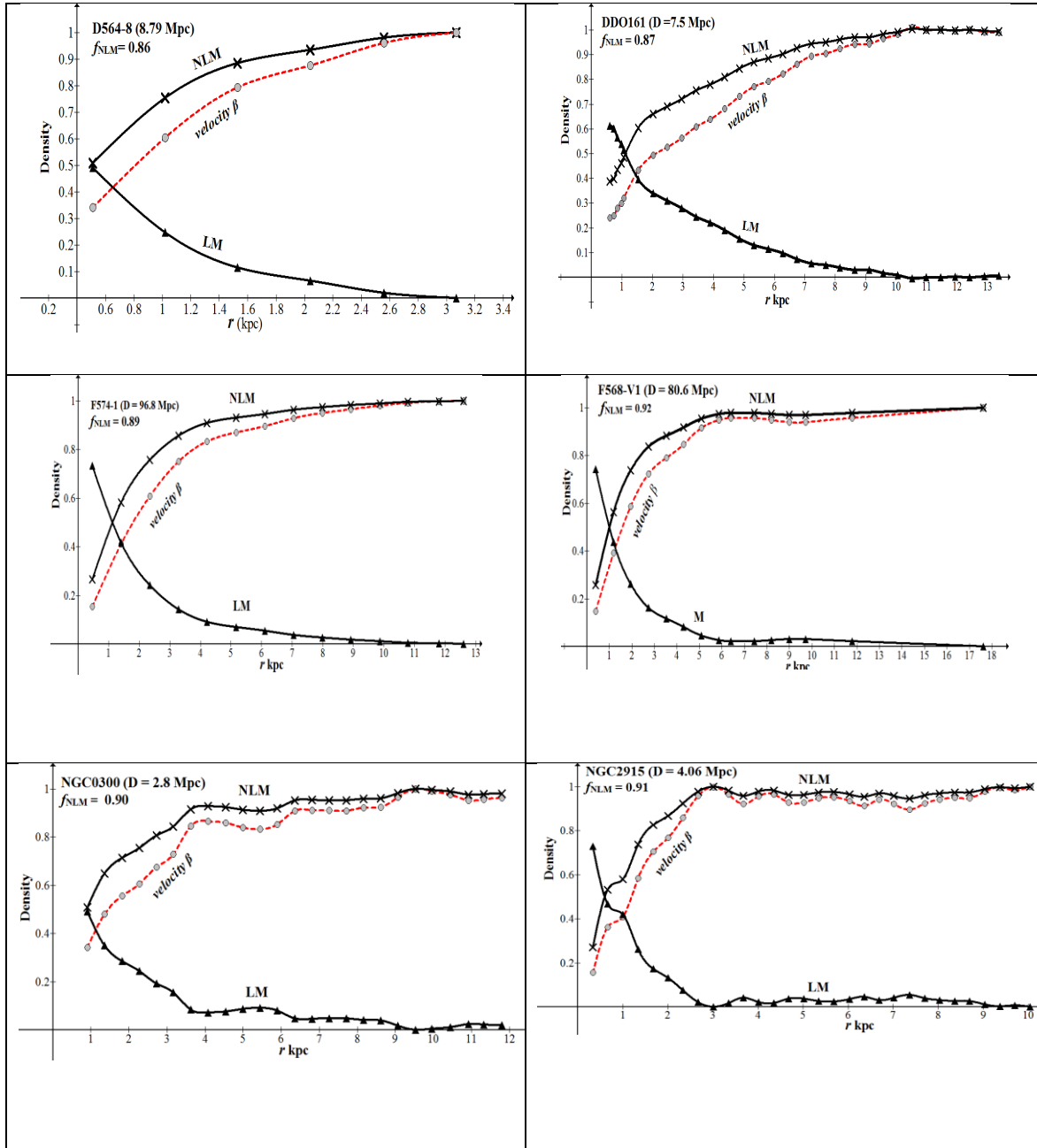


Figure 3. Predicted radial density distributions of luminous and nonluminous matter for six galaxies, alongside with their respective measured rotational curves (the plots for all the investigated galaxies appear in Appendix A).

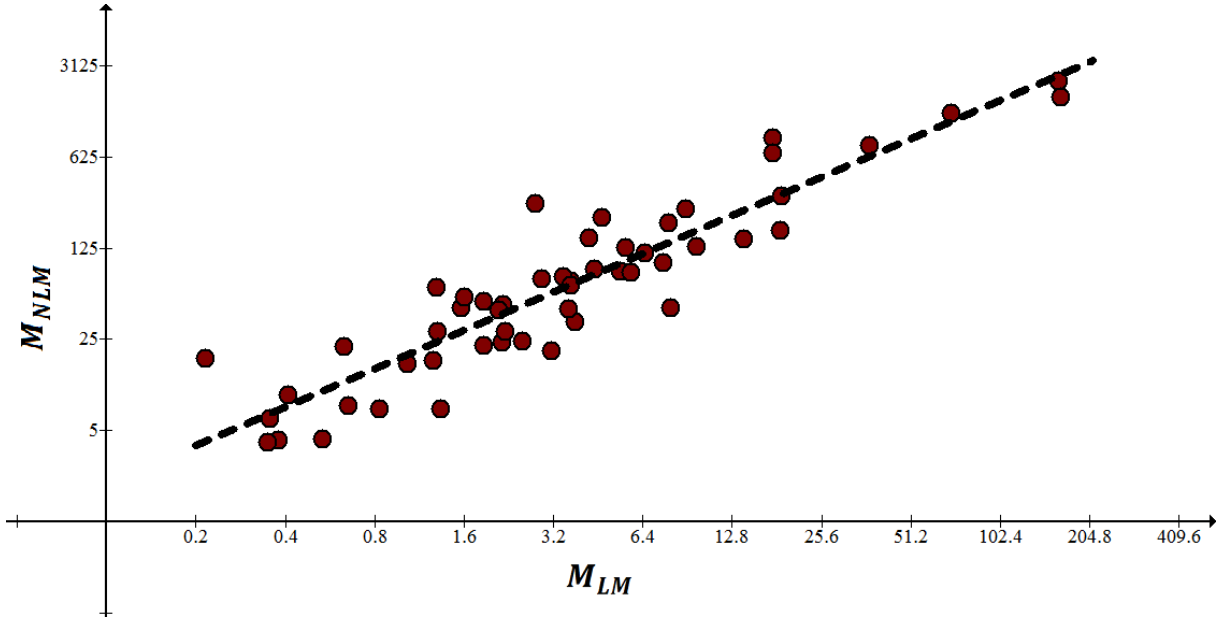


Figure 4. The predicted relation between the masses of the nonluminous and the luminous components for 52 SPARC galaxies.

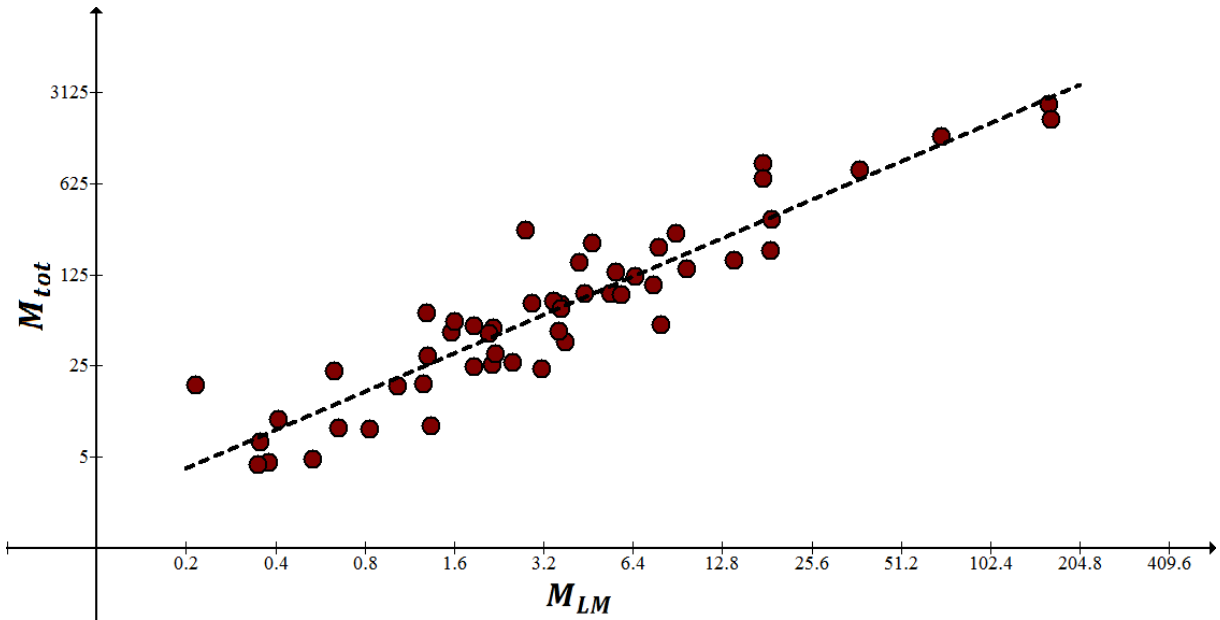


Figure 5. The predicted relation between the total dynamical mass and the luminous component mass for 52 SPARC galaxies.

4. Summary and main conclusion

In previous papers [46][47], we analyzed the relativistic effects caused by the departure of a body of mass from a stationary observer. Applying these analyses to cosmology has successfully predicted and explained several phenomena, including the GZK cutoff in the cosmic-ray energy spectrum, the coincidence problem, and the deceleration-acceleration transition redshift.

Notably, the results suggest that the mysterious dark energy might be the energy of the nonluminous component of the receding universe.

In this paper, we utilized the dynamical equivalence between rectilinear and circular motion [48] to derive relativistic terms for the luminous and nonluminous matter components of a homogeneous, uniformly rotating disk. Under simplifying assumptions, we applied these results to construct the radial distributions of luminous and nonluminous matter in 52 diverse disk galaxies, randomly selected from the SPARC database.

Our investigation of the resulting distributions revealed that the features attributed to dark matter particles in galaxy halos are accounted for by our proposed relativistic model. These features are extractable solely from the measured rotation curves of the galaxies. Specifically, the model successfully reproduces the main and well-confirmed characteristics of nonluminous matter in galaxies, including its dominance over ordinary matter, its concentration in the galaxies' outskirts, its strong coupling with ordinary matter [34][35][36][37], and the Baryonic Tully-Fisher relation [67][68]. The model does not suffer from a “cusp” problem [33]. It also aligns with the indefinitely flat circular velocity observations [40], since unlike the CDM paradigm, which presumes bounded regions with defined radii where dark matter is clumped, our duality model suggests a continuous buildup of the nonluminous component, broadly defining the halo as the region where the bulk of matter becomes nonluminous.

In conclusion, we suggest that the darkness of galaxy halos is a relativistic phenomenon governed by the galaxies' rotational velocities, rather than the presence of exotic, undiscovered "dark matter particles."

References

1. Roberts, M. S., & Whitehurst, R. N. The rotation curve and geometry of M31 at large galactocentric distances. *ApJ* **1975**, 201, 327-346.
2. Rubin, V. C., Ford, W. K. Jr., & Thonnard, N. Extended rotation curves of high-luminosity spiral galaxies. IV - Systematic dynamical properties, SA through SC, *ApJL* **1978**, 225, L107.
3. Rubin, V. C., Ford, W. K. Jr., & Thonnard, N. Rotational properties of 21 SC galaxies with a large range of luminosities and radii, from NGC 4605 /R = 4kpc/ to UGC 2885 /R = 122 kpc, *ApJ* **1980**, 238, 471- 487.
4. Sofue, Y., & Rubin, V. C. Rotation curves of spiral galaxies, *ARA&A* **2001**, 39, 137.
5. Drew, P. M., et al. Evidence of a Flat Outer Rotation Curve in a Star-bursting Disk Galaxy at $z = 1.6$. *ApJ* **2018**, 869 58.
6. Sofue, Y. Rotation Curve of the Milky Way and the Dark Matter Density. *Galaxies* **2020**, 8, 37. <https://doi.org/10.3390/galaxies8020037>.
7. Teodoro, E. M. Di, et al. Dark matter halos and scaling relations of extremely massive spiral galaxies from extended HI rotation curves, *MNRAS* **2023**, 518 (4), 6340–6354.
8. Schneider, P. Detection of (dark) matter concentrations via weak gravitational lensing, *MNRAS* **1996**, 283 (3), 837–853.
9. Wittman, D., Tyson, J., Kirkman, D. et al. Detection of weak gravitational lensing distortions of distant galaxies by cosmic dark matter at large scales. *Nature* **2000**, 405, 143–148.
10. Wallis, C.G.R., et. al, Mapping dark matter on the celestial sphere with weak gravitational lensing. *MNRAS* **2022**, 509 (3), 4480-4497.
11. Croon, D., McKeen, D., & Raj, N. Gravitational microlensing by dark matter in extended structures, *Phys. Rev. D* **2020**, 101, 083013.
12. Tambalo, G., et al. Gravitational wave lensing as a probe of halo properties and dark matter. *Phys. Rev. D* **2023**, 108, 103529.

13. Dekel, A., Stoehr, F., Mamon, G. et al. Lost and found dark matter in elliptical galaxies. *Nature* **2005**, 437, 707–710.
14. McDaniel, A., Jeltema, T., & Profumo, S. X-ray shapes of elliptical galaxies and implications for self-interacting dark matter, *JCAP* **2021**, 5, 2021 004.
15. Sohn, J. et al. Velocity dispersions of quiescent galaxies in IllustrisTNG. *APJ* **2024**, 964:178 (11pp).
16. Barack, L., et al. White Paper for the COST action “Gravitational Waves, Black Holes, and Fundamental Physics” (269 pages), arXiv:1806.05195 (**2018**).
17. Bergström, L. Non-baryonic dark matter: observational evidence and detection methods. *Rept. Prog. Phys.* **2000**, 63 (5), 793.
18. Bertone, G., Hooper, D., & Silk, J. Particle dark matter: Evidence, candidates and constraints. *Phys. Rept.* **2005**, 405, 279–390.
19. Feng, L. L. Dark matter candidates from Particle physics and methods of detection. *Ann. Rev. Astron. Astrophys.* **2010**, 48, 495–545.
20. Steigman G., Turner M. S. Cosmological constraints on the properties of weakly interacting massive particles. *Nuclear Physics B* **1985**, 253, 375-386.
21. Sivertsson S., Gondolo P. The WIMP capture process for dark stars in the early Universe. *Astrophys. J.* **2011**, 729, 51 [11pages]
22. Aprile E., et al. Dark matter results from 100 live days of XENON100 data. *Phys. Rev. Lett.* **2011**, 107, 131302 [6 pages].
23. Roszkowski, L., et al. WIMP dark matter candidates and searches—current status and future prospects. *Rep. Prog. Phys.* **2018**. 81 066201.
24. Alcock C. EROS and MACHO combined limits on planetary-mass dark matter in the galactic halo. *ApJ* **1998**, 499, 9– 12.
25. Alcock C. MACHO project limits on black hole dark matter in the 1-30 solar mass range. *ApJL* **2001**, 550 (2), 169–172.
26. Graham, P. W., & Ramani, H. Constraints on dark matter from dynamical heating of stars in ultrafaint dwarfs. Part 1: MACHOs and primordial black holes. <https://arxiv.org/abs/2311.07654> (**2023**).
27. Carr, B., Kuhnel, F., & Sandstad, M. Primordial black holes as dark matter. *Phys. Rev. D* **2016**, 94, 083504.
28. Carr, B., & Kühnel, F. Primordial Black Holes as Dark Matter: Recent Developments *Ann. Rev. Nucl. Part. Sci.* **2020**. 70:355–94.
29. Pérez de los Heros, C. Status, Challenges and Directions in Indirect Dark Matter Searches. *Symmetry* **2020**, 12, 1648.
30. Billard, J., et al. Direct detection of dark matter - APPEC committee report. *Rep. Prog. Phys.* **2022**, 85 056201.
31. Misiaszek, M.; Rossi, N. Direct Detection of Dark Matter: A Critical Review. *Symmetry* **2024**, 16, 201.
32. Ricardo A. Flores, Joel R. Primack. Observational and theoretical constraints on singular dark matter halos. *Astrophys. J.* **1994**, 427, L1-4
33. Del Popolo, A.; Le Delliou, M. Review of Solutions to the Cusp-Core Problem of the Λ CDM Model. *Galaxies* **2021**, 9, 123.
34. Lelli, F., et al. SPARC: Mass models for 175 disk galaxies with spitzer photometry and accurate rotation curves, *A.J.* **2016**, 152, 157.
35. McGaugh, S. S., Lelli, F., & Schombert, J. M. Radial Acceleration Relation in Rotationally Supported Galaxies. *Phys. Rev. Lett.* **2016**, 117, 201101.
36. Lelli, F., McGaugh, S.S., Schombert, J.M., & Pawlowski, M.S. One law to rule them all: The radial acceleration relation of galaxies. *APJ* **2017**. 836:152 (23pp).
37. Li, P., Lelli, F., McGaugh, S., & and Schormbert, J. Fitting the Radial Acceleration Relation to Individual SPARC Galaxies, *Astron. Astrophys* **2018**. 615, A3.

38. Scholz-Díaz, L., Martín-Navarro, I., Falcón-Barroso, J. et al. Baryonic properties of nearby galaxies across the stellar-to-total dynamical mass relation. *Nat. Astron.* **2024**, 1-9.
39. Walcher, C. J. et al. CALIFA: a diameter-selected sample for an integral field spectroscopy galaxy survey. *A & A* **2014**, 569, A1.
40. Mistele, T. *et al.* Indefinitely flat circular velocities and the baryonic Tully–Fisher relation from weak lensing. *ApJL* **2024**, 969 L3.
41. L. D. Bradley et al. High-redshift galaxy candidates at $z=9-10$ as revealed by JWST observations of WHL0137-08. *ApJ* **2023**, 955:13 (15pp).
42. Adams, N. J., et al. Discovery and properties of ultra-high redshift galaxies ($9 < z < 12$) in the JWST ERO SMACS 0723 Field. *MNRAS* **2023**, 518, 4755–4766
43. Glazebrook, K., Nanayakkara, T., Schreiber, C. *et al.* A massive galaxy that formed its stars at $z \approx 11$. *Nature* **628**, 277–281 (2024).
44. Behroozi, P. & Silk, J. The most massive galaxies and black holes allowed by Λ CDM. *Mon. Not. R. Astron. Soc.* **477**, 5382 – 5387 (2018).
45. Boylan-Kolchin, M. Stress testing Λ CDM with high-redshift galaxy candidates. *Nature Astronomy* **7**, 731–735 (2023)
46. Suleiman, R. A model of dark matter and dark energy based on relativizing Newton’s physics. *WJCMF* **2018**, 8, 130-155.
47. Suleiman, R. A local-deterministic alternative to quantum gravity. Paper presented at the XII International Conference on New Frontiers in Physics (ICNFP), OAC, Kolymbari. Crete, Greece, 10-23 July, **2023**. DOI: [10.13140/RG.2.2.14347.67365](https://doi.org/10.13140/RG.2.2.14347.67365).
48. Suleiman, R. Circular and rectilinear Sagnac effects are dynamically equivalent and contradictory to special relativity theory. *Phys. Essays* **2018**, 31 (2), 215-218.
49. Suleiman, R. *Relativizing Newton* (Nova Science Publishers. N.Y, **2019**).
50. Suleiman, R. Spatial locality is the hidden variable in entanglement experiments. *Phys. Essays* **2016**, 29, 503-505.
51. Suleiman, R. A relativistic model of matter-wave duality explains the results of the double-slit experiment. Poster presented at the 5th. International Conference on New Frontiers in Physics ICNFP2016, Kolymbari, Crete, July **2016**.
52. Kalman, R. *Mathematical description of linear dynamical systems, J.S.I.A.M.: Control* **1963**, 1 (2), 152-192.
53. Ogata, K. *System Dynamics* (Prentice Hall, 4th. Edition, **2003**).
54. Drake, S. *Discoveries and Opinions of Galileo* (Doubleday Anchor, New York, 113–114. **1957**).
55. Chalmers, A. Galilean relativity and Galileo’s relativity. In: *Correspondence, Invariance and Heuristics: Essays in Honor of Heinz Post*. S. French, & H. Drake, S. *Discoveries and Opinions of Galileo* (Doubleday Anchor, New York, 113–114. **1957**).
56. Olsen S. *The Golden Section* (New York, Walker & Co., **2006**).
57. Douady, S., Couder, Y. Phyllotaxis as a physical self-organizing growth process. *PRL* **1992**, 68 (13), 2098- 2101.
58. Coldea R., et al. Quantum criticality in an Ising chain: Experimental evidence for emergent E8 symmetry. *Science* **2010**, 327 (5962), 177–180.
59. Stoudenmire E. M., Clarke D. J., Mong R. S., K., and Alicea, J. Assembling Fibonacci anyons from a Z_3 parafermion lattice model. *Phys. Rev. B* **2015**, 91, 235112.
60. Heyrovska, R. The Golden ratio, ionic and atomic radii and bond lengths. *Mol. Phys.* **2005**, 103, (6-8), 877–882.
61. Lindner, J.F., et al. Strange Nonchaotic Stars. *Phys. Rev. Lett* **2015**, 114.
62. Marples, C.R.; Williams, P.M. The golden ratio in nature: A tour across length scales. *Symmetry* **2022**, 14, 2059. <https://doi.org/10.3390/sym14102059>.
63. Pletser, V. Fibonacci numbers and the golden ratio in biology, physics, astrophysics, chemistry and technology: A non-exhaustive review. arXiv:1801.01369 (**2017**).

64. Gentile, G. et al. NGC 3741: dark halo profile from the most extended rotation curve. *MNRAS* **2007**, 375 (1), 199 - 212.
65. Banerjee, A., et al. A slow bar in the dwarf irregular galaxy NGC 3741. *MNRAS* **2013**, 434, 1257–1263.
66. Graph <https://www.padowan.dk/download/>
67. McGaugh, S. S. Schombert, J. M., Bothun, G. D., and de Blok, W. J. G. The baryonic Tully-Fisher relation. *ApJ* **2000**, 533, L99.
68. Pfenniger, D., and Revaz, Y. The Baryonic Tully-Fisher relation revisited. *A&A* **2005**, 431, 511–516.

Appendix A

Predicted radial distributions of the luminous and nonluminous matter for 52 SPARC galaxies, alongside with their measured rotation curves

